

Transition region and coronal structuring

E. O’Shea¹, P.T. Gallagher^{1,2}, M. Mathioudakis¹, K.J.H. Phillips², F.P. Keenan¹, and A.C. Katsiyannis¹

¹ Department of Pure and Applied Physics, The Queen’s University of Belfast, Belfast, BT7 1NN, N. Ireland (E.Oshea@qub.ac.uk; P.Gallagher@qub.ac.uk; M.Mathioudakis@qub.ac.uk; F.Keenan@qub.ac.uk; A.Katsiyannis@qub.ac.uk)

² Space Science Department, Rutherford Appleton Laboratory, Chilton, Didcot, Oxon. OX11 0QX, UK (phillips@solg2.bncs.rl.ac.uk)

Received 27 August 1999 / Accepted 17 February 2000

Abstract. In this paper we examine regions of internetwork, network and bright network emission, observed in the quiet Sun with the Coronal Diagnostic Spectrometer (CDS) onboard SoHO. The slopes of the emission measure distributions, between $5.4 \leq \log T_e \leq 6.0$, are found to differ in each region, suggesting the presence of different atmospheric structures. From an analysis of emission area the network is shown to have two populations of structures, a low transition region group and a coronal group. Using MDI magnetograms the bright network emission is shown to originate from regions of strong magnetic field composed of bipolar loops and unipolar funnels, that extend from the low transition region up to the corona. Up to 30% of all radiative losses between $5.7 \leq \log T_e \leq 6.3$ are found to come from these continuous bright network structures. Cross-sectional areas calculated from redshift values suggest that the area expansion seen in the bright network emission is the result of flux tube expansion into the corona, accompanied by either a downflow or upflow of material.

Key words: techniques: image processing – methods: observational – Sun: corona – Sun: transition region – Sun: UV radiation – Sun: atmosphere

1. Introduction

The simplest picture of the transition region, formed between temperatures of $\sim 10^4\text{K}$ and 10^6K , is that it is the thermal interface between the hot corona and the cooler chromosphere, and that it is heated by a process of back heating. Early models of the transition region assumed a plane-parallel geometry. However, following Gabriel (1976) these simple energy balance models were modified to include the effect of a magnetic field that expanded and fanned out at coronal heights. This model and later ones (e.g. Athay, 1981, 1982) implicitly include the assumption that the magnetic field within the network is unipolar over supergranular scales. Dowdy et al. (1986) have argued that the observed fine scale structure of the network, consists of mixed magnetic polarities. This led them to propose an alternative ‘magnetic junkyard’ picture of the transition region, consisting of coronal funnels and small cool network loops.

It has been proposed (Habbal et al. 1990) that bright points in the network boundaries are formed from a complex of loop structures at different temperatures, which are a subset of the small-scale network loops proposed by Dowdy et al. Habbal & Grace (1991) argue that these bright points show two favoured temperature distributions (of closed magnetic structures) in the quiet Sun, one below $3 \times 10^5\text{K}$, and one at coronal temperatures, implying that not all structures in the quiet Sun reach coronal temperatures. Dowdy (1993) suggests that bright points without associated coronal brightenings can be interpreted as network loops that are heated internally but which have no strong thermal connection to the large-scale corona. Similarly he suggests that bright points that have associated coronal brightenings, i.e. coronal bright points, are network loops that have been heated to coronal temperatures but which are still insulated from the large-scale corona by their magnetic fields.

Early investigations of the quiet Sun with the Skylab S055 instrument (Reeves, Vernazza & Withbroe, 1976) indicated that the intensity histogram of EUV features follows a distribution in which there is a strong peak at a relatively low intensity and a tail extending to several times the peak intensity. Vernazza, Avrett & Loeser (1981) found that up to six different features such as dark points within the internetwork, bright network elements, average network emission etc. could be characterised from the intensity distribution. Using a number of transition region and coronal lines Gallagher et al. (1998) separated intensity distributions into internetwork and network regions and examined the variation of different network properties with temperature. They found that the transition region model of Gabriel, i.e. that the network fans out in the form of a funnel at coronal heights, is consistent with their results. Recently Patsourakos et al. (1999) examined the expansion of network boundaries with temperature and found similar results.

In this paper we use Coronal Diagnostic Spectrometer (CDS) and Michelson Doppler Imager (MDI) observations to study the internetwork and network emission in the quiet Sun. Following Vernazza, Avrett & Loeser (1981) and expanding on the work of Gallagher et al. (1998), we propose that the quiet Sun intensities can be separated into three distributions; the internetwork, the ‘normal’ network and the bright network. We focus our analysis primarily on the network and bright network emission and

Table 1. Details of the high telemetry INT_DIST observing sequence.

| | |
|----------------------------|--------------------------------------|
| Date of observation | 11 April |
| Time of observation | 08:42 UT |
| Instrument | CDS/NIS |
| Slit size on Sun | 4×240 arcsec ² |
| Wavelength covered by slit | ~ 2.8 Å |
| Exposure time | 40 sec |
| Number of slit positions | 60 |
| Area imaged | 240×240 arcsec ² |
| Total duration | 55 minutes |

it's variation with temperature. We present the results of this analysis in Sect. 3 and the conclusions in Sect. 4.

2. Observations and data reduction

2.1. Observations

The EUV observations were obtained with the Coronal Diagnostic Spectrometer (Harrison et al. 1995) operating in *high telemetry* mode. The observing sequence INT_DIST (see Table 1) was designed primarily to provide CDS/NIS (Normal Incidence Spectrometer) images of the quiet Sun at disc centre in nineteen wavelength regions. The lines identified together with the maximum temperature of formation, are given in Table 2. The data were corrected for cosmic ray events, CCD readout bias, pixel-to-pixel variations and tilted spectral lines. This was done using the standard CDS/NIS calibration software. A radiometric calibration was also performed to convert the original photon count rates into ergs cm⁻² s⁻¹ sr⁻¹ Å⁻¹. Note that we did not use the full 240 pixels in the Solar-Y direction. It was necessary to remove the top 37 pixels due to a small brightening event occurring at this location.

Using the Michelson Doppler Imager (MDI) (Scherrer et al., 1995) magnetograms were also obtained at 08:44 UT on 11 April. MDI was operating in the high resolution mode. In this mode 10 arcmin \times 10 arcmin images with a spatial resolution of 1–2 arcsec were taken at the same location as the CDS observations.

2.2. Image segmentation

In this section we expand upon previous image segmentation algorithms discussed by Gallagher et al. (1998). We use a histogram modification technique based on detecting pixels within the images which show high edge values (Weszka & Rosenfeld, 1979; Gupta & Sortrakul, 1998).

We assume that the image consists of three components; internetwork, network, and bright network, each having a unimodal grey-level intensity distribution. Therefore, the intensity histogram of the total image will be a mixture of three unimodal histograms. The choice of three distributions seems reasonable as the quiet Sun has been shown to contain not only the internetwork and network components (Gallagher et al., 1998), but also an enhanced network or bright point component (Dowdy, 1993). Habbal & Grace (1991) find that the enhanced emission

Table 2. The lines identified in the observing sequence INT_DIST.

| Ion | Transition | Wavelength | log(T _e) |
|----------|--|------------|----------------------|
| He I | $1s^2 \ ^1S_0 - 1s2p \ ^1P_1$ | 584.33 | 4.50 |
| He II | $1s \ ^2S_{1/2} - 2p \ ^2P_{1/2,3/2}$ | 303.78 | 4.90 |
| O III* | $2s^2 2p^2 \ ^1D_2 - 2s2p^3 \ ^1P_1$ | 525.80 | 5.10 |
| Ne IV* | $2s^2 2p^3 \ ^4S_{3/2} - 2s2p^4 \ ^4P_{5/2}$ | 543.89 | 5.30 |
| O IV* | $2s^2 2p \ ^2P_{3/2} - 2s2p^2 \ ^2P_{3/2}$ | 554.52 | 5.30 |
| O V* | $2s^2 \ ^1S_0 - 2s2p \ ^1P_1$ | 629.73 | 5.40 |
| Ne VI | $2s^2 2p \ ^2P_{1/2} - 2s2p^2 \ ^2D_{3/2}$ | 558.59 | 5.60 |
| Ne VI* | $2s^2 2p \ ^2P_{3/2} - 2s2p^2 \ ^2D_{5/2}$ | 562.80 | 5.60 |
| Ne VII* | $2s2p \ ^3P_2 - 2p^2 \ ^3P_2$ | 561.73 | 5.70 |
| Ca X* | $3s \ ^2S_{1/2} - 3p \ ^2P_{3/2}$ | 557.76 | 5.80 |
| Mg VIII | $2p \ ^2P_{1/2} - 2s2p^2 \ ^2P_{1/2}$ | 313.75 | 5.90 |
| Si VIII | $2s^2 2p^3 \ ^4S_{3/2} - 2s2p^4 \ ^4P_{1/2}$ | 314.33 | 5.90 |
| Si VIII* | $2s^2 2p^3 \ ^4S_{3/2} - 2s2p^4 \ ^4P_{5/2}$ | 319.83 | 5.90 |
| Mg IX* | $2s^2 \ ^1S_0 - 2s2p \ ^1P_1$ | 368.07 | 6.00 |
| Mg X* | $2s \ ^2S_{1/2} - 2p \ ^2P_{1/2}$ | 624.94 | 6.05 |
| Si X* | $2p \ ^2P_{1/2} - 2s2p^2 \ ^2D_{3/2}$ | 347.40 | 6.10 |
| Fe XIII | $3s^2 3p^2 \ ^3P_2 - 3s3p^3 \ ^3P_2$ | 320.80 | 6.20 |
| Fe XIII* | $3s^2 3p^2 \ ^3P_0 - 3s3p^3 \ ^3D_1$ | 348.18 | 6.20 |
| Fe XIII | $3s^2 3p^2 \ ^3P_1 - 3s3p^3 \ ^3D_2$ | 359.64 | 6.20 |
| Fe XV | $3s3p \ ^3P_2 - 3p^2 \ ^3P_1$ | 321.80 | 6.30 |
| Fe XV | $3s3p \ ^3P_2 - 3p^2 \ ^1D_2$ | 327.03 | 6.30 |
| Fe XVI* | $3s \ ^2S_{1/2} - 3p \ ^2P_{3/2}$ | 335.41 | 6.30 |
| Fe XVI* | $3s \ ^2S_{1/2} - 3p \ ^2P_{1/2}$ | 360.79 | 6.30 |

[†]Lines marked by asterisks are those used to construct the differential emission measures

covers between 10 and 25% of the surface depending on the temperature. In most situations a threshold level between each of the populations can be difficult to detect due to the fact that they are not well separated in intensity.

There are several methods that can be used to produce a transformed grey-level histogram in which the valley between populations is deeper, and is thus easier to detect. Suppose we have an image, $I(x, y)$, composed of three regions closely grouped in intensity. We can use the Laplacian operator to detect the threshold between populations. In a continuous image the Laplacian operator

$$\nabla^2 I(x, y) = \frac{\partial^2 I(x, y)}{\partial x \partial y} \quad (1)$$

forms a second partial derivative of the image. In regions where there is little or no variation in intensity, the absolute value of the Laplacian is zero while large values occur on the borders between objects. The histogram of high Laplacian points should therefore have two peaks, representing the internetwork–network boundary (T_1) at low intensities and the network–bright network boundary (T_2) at high intensities (see Fig. 1).

The Laplacian modified histogram can then be fitted with two Gaussians in order to establish the thresholding levels to be used in pixel classification. In our case the following classification rules are then applied;

$$(x, y) = \begin{cases} \text{internetwork} & \text{if } I(x, y) < T_1, \\ \text{network} & \text{if } T_1 \leq I(x, y) \leq T_2, \\ \text{bright network} & \text{if } I(x, y) > T_2. \end{cases} \quad (2)$$

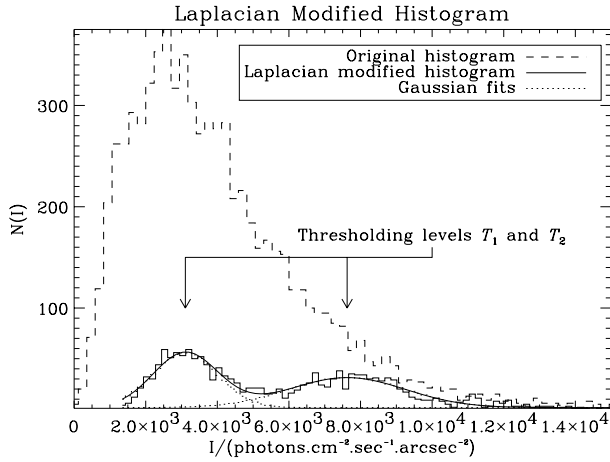


Fig. 1. The original and Laplacian transformed histograms for the $240'' \times 240''$ O V (629.73 \AA) image. The threshold levels for the internetwork–network (T_1) and network–bright network boundaries (T_2) are also shown.

3. Results and discussion

3.1. Emission measure distributions

A widely used method for the analysis and interpretation of solar observations is based on differential emission measure distributions (DEM), e.g. Raymond & Doyle (1981). In the present study differential emission measures were produced using the CHIANTI software package (Del Zanna et al., 1997, Dere et al., 1997), the ionization equilibrium values of Arnaud & Rothenflug (1985) and the coronal abundances of Feldman et al. (1992). The DEM is given by:

$$DEM(T) = N_e^2(T) \frac{dh}{dT} \text{ cm}^{-5} \text{K}^{-1} \quad (3)$$

where $N_e(T)$ is the electron density, and dh/dT is the reciprocal of the line of sight temperature gradient. We found it necessary to increase the abundance of oxygen by 0.2 dex, in order to obtain consistency between the oxygen and neon spectral lines.

Despite the large number of lines observed, several of these were unsuitable for DEM analysis due to blending problems or low intensities. For example, Ne VI 558.59 \AA is blended with Ne VII 558.609 \AA while Fe XV 327.03 \AA was found to have a low intensity in all the regions. The two helium lines are not used as they are both optically thick.

The emission measures produced using the remaining lines are shown in Fig. 2 for the internetwork, network and bright network areas. The differential emission measures are plotted versus the temperature where the product of the $G(T)$ function and the DEM is at a maximum. Note that the Ne VII 561.73 \AA line is absent from both the internetwork and network regions.

Raymond and Doyle (1981) found that, assuming a power law of the form $EM \sim T^\alpha$, the emission measures for the network and internetwork had slopes (α) of 1.4 and 2.1 respectively. Recently, Griffiths et al. (1999) found that this slope varied from between ~ 1.8 in the highest intensity regions up to ~ 2.4 in the lowest intensity regions, for temperatures in the range of 5.2

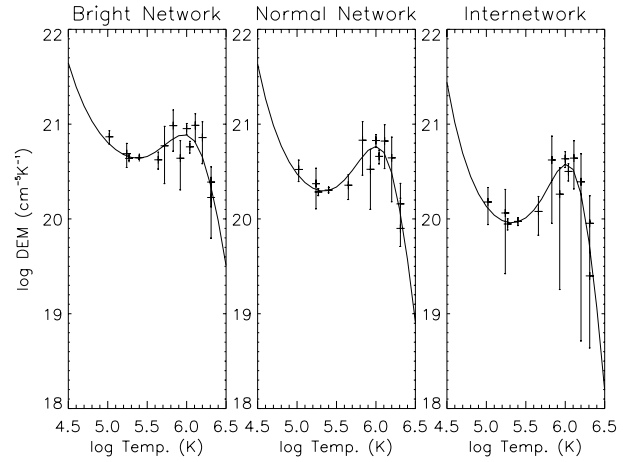


Fig. 2. Differential emission measures of (from left to right) the bright network, the network and the internetwork region. Temperatures shown are the product of $G(T) \times DEM(T)$.

$\leq \log T_e \leq 6.2$. Griffiths et al. argue that the trend of these results suggests a decrease in the emission measure slope with increasing intensity. Applying the same technique to our results we find slopes of 1.3 for the bright network, 1.6 for the network and 1.8 for the internetwork, between temperatures of $5.4 \leq \log T_e \leq 6.0$. We also see a decrease in slope with increasing intensity, with the bright network region showing the lowest value of α , although there may be some abundance related uncertainties in these values. Following the argument of Griffiths et al. (1999) these results suggest that different density structures are contributing to each internetwork and network region.

3.2. Filling factors of the emission

One of the outcomes of the image segmentation technique, is that it allows us to estimate the percentage area (spatial density) occupied by the internetwork, network and bright network emission in each line. In Fig. 3 we plot these area percentages as a function of the line formation temperature. Each of the distributions has been fitted with a second order polynomial.

Fig. 3(a) indicates that the area of network emission does not change significantly with temperature, with only a marginal decrease towards higher temperatures. However an examination of the rasters of eight representative low and high temperature lines, shown in Fig. 4, indicates that the network shape changes considerably at or about the temperature of the Ne VII line. This is despite the fact that the overall percentage area of network emission remains more or less constant. Feldman (1987) used the fact that the network in low and high temperature lines is very different in appearance, e.g. O III and Si X in our figure, to argue that unresolved fine structures extend in temperature up to at least that of the Ne VII line, but not to coronal temperatures.

In Fig. 3 the internetwork emission area shows a maximum increase at the temperature of the Ne VI and Ne VII lines. In comparison the combined network area (i.e. the area of emission from the normal and bright network) shows a minimum at the temperatures of Ne VI and Ne VII, before increasing again to

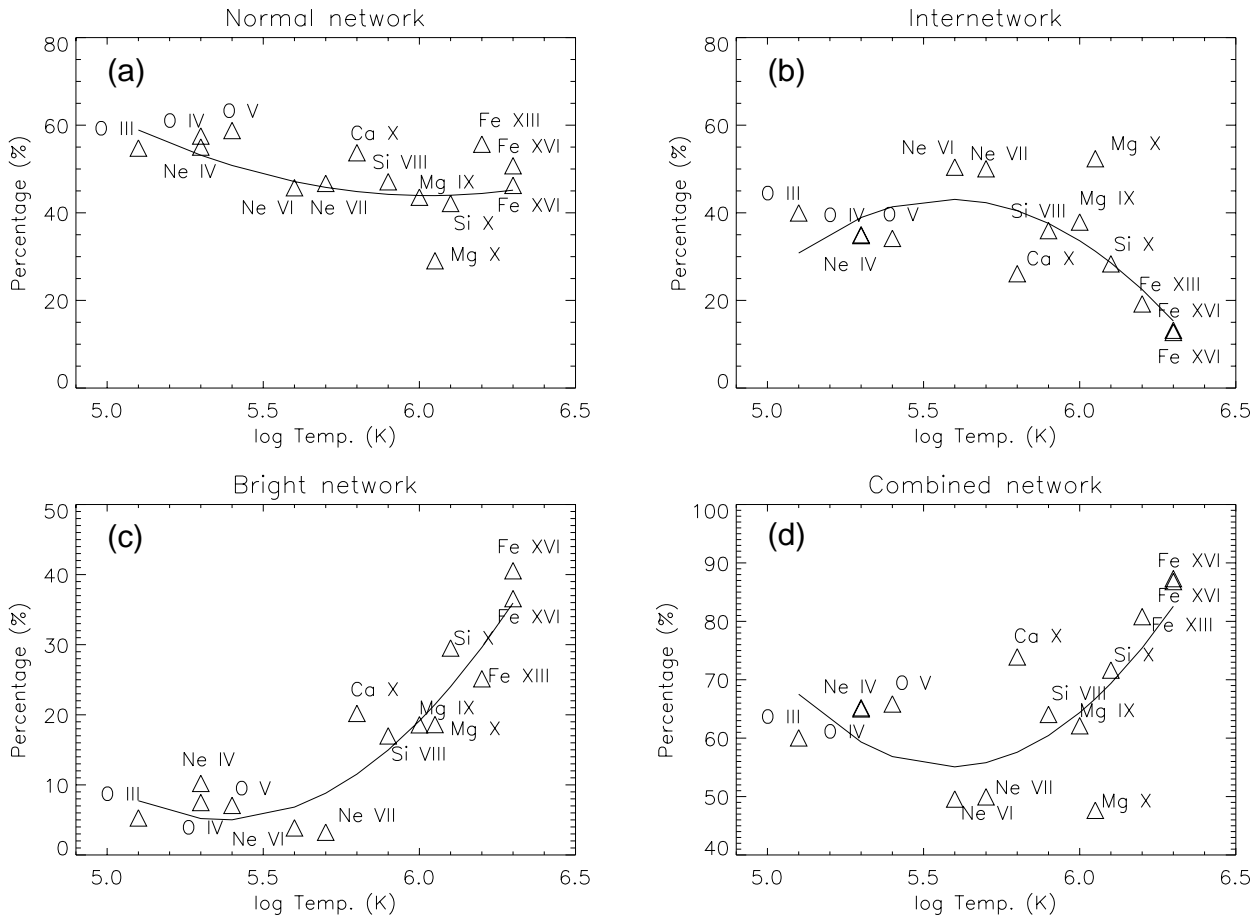


Fig. 3a – d. Percentage of **a** normal network emission, **b** internetwork emission, **c** bright network emission, and **d** combined network (normal network and bright network) emission.

reach a maximum at the temperature of Fe XVI. Habbal & Grace (1991) interpreted a similar minimum in their estimates of spatial densities to indicate that within the structure of bright points there exist two favoured temperature populations of magnetic structures: one below 3×10^5 K and one at coronal temperatures. We argue that our results also show the presence of two populations within the (combined) network, a low transition region group and a coronal group. However, we must be careful in making these assumptions as our technique for separating the areas can assign a non-negligible number of pixels to the wrong distribution. While this technique still gives a valid estimate of the proportion of area in each distribution it can produce some uncertainties. An examination of the rasters plotted in Fig. 4, confirms that there is a minimum in the amount of network area at the temperature of Ne VII. It is also possible to see from these rasters that the amount of network area decreases from larger values at low temperatures to increase again at higher temperatures, albeit with a different appearance. This increase in network area at higher temperatures has been taken to signify the opening out of flux tubes or funnels (Gallagher et al., 1998, Patsourakos et al., 1999).

We note that the Ca X and Mg X lines show slightly anomalous values for the amount of combined network and internet-

work area. For example, Mg X shows a value that is significantly smaller than the values of other coronal lines in the combined network plot, while Ca X shows a value significantly higher than similar temperature lines, such as Si VIII. These variations are possibly explained by the fact that both lines are blended to a small degree, Mg X with a line of O IV 624 Å and Ca X with the Ne VI 558 Å line. These values should therefore be treated with some caution.

A plot of bright network emission, Fig. 3(c), shows a rapid increase in the area above a temperature of $\log T_e = 5.7$ K. Again this can be qualitatively confirmed by examining the rasters in Fig. 4. Some bright points (e.g. at X=160, Y=70 arcsec) in this figure show no appreciable expansion with temperature, but overall the rapid expansion of the bright network to higher temperatures indicates the opening out of flux tubes, either in the form of funnels or loop structures into the corona. In order to examine the magnetic structure of the network we use an MDI magnetogram which was taken on the same day as the CDS observations (see Sect. 2.1). This is plotted in Fig. 5. We have overlain the magnetogram with bright network contours of O V and Si VIII in black and normal network contours of the same lines in white. In the magnetogram the intensity has been scaled to ± 50 G to bring up the weaker field structure. Mag-

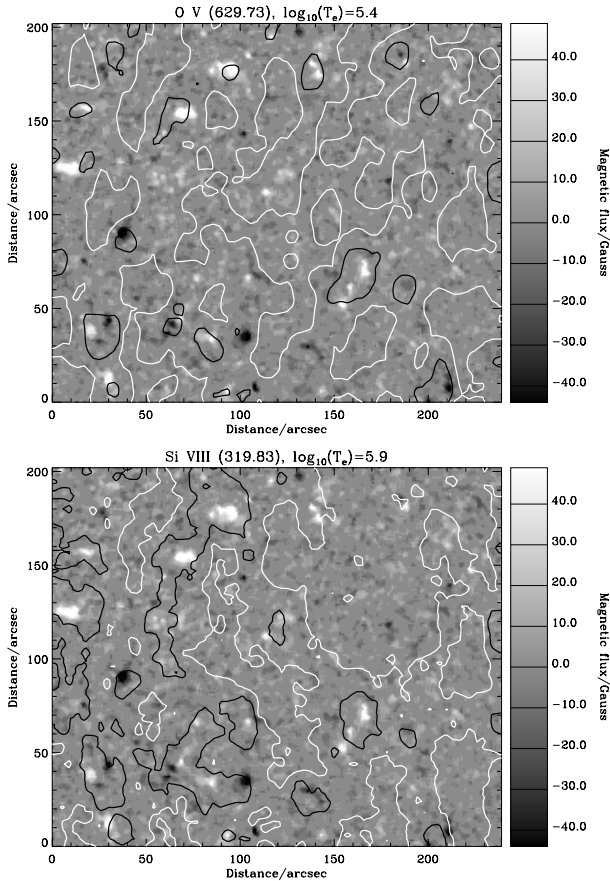


Fig. 5. High-resolution MDI magnetograms showing the field concentrations in the quiet Sun. The magnetogram has been scaled to highlight weaker magnetic features. In the upper panel the magnetogram has been contoured with the O V (629 Å) bright network (black lines) and normal network (white lines) while the bottom panel shows the corresponding Si VIII (319 Å) contours.

netic fields with values greater than this will thus be saturated in these images, appearing as either purely black or white, depending on their polarity. In Table 3 we show the distribution of magnetic field within the bright network, normal network and internetwork areas defined using the O V contours. The maximum magnetic field per pixel is 330.7 Gauss. It can be seen that almost 70% of the total magnetic field lies within the bright and normal network.

It is striking that the bright network emission in both the O V and Si VIII lines is concentrated precisely in those areas where there is a strong magnetic field, as indicated by the black and white patches. Note that the (coronal) bright point at approximately $X=160$, $X=70$ arcsec (160,70) corresponds to a strong unipolar magnetic region. No strong opposite magnetic polarity is visible. Similar bright network points are apparent at (60, 150), (40,85) and (95, 175). The area of emission over these bright points increases in the Si VIII line, signifying the opening out of a coronal funnel. As this magnetogram was obtained less than two minutes after the raster images, the magnetic structure did not have time to change significantly. These brightenings may be due to local density enhancements, caused by localized

heating, along individual field lines emanating from patches of purely unipolar magnetic flux. In these regions there appear to be no magnetic bipoles present. This is in contradiction to the arguments of Dowdy (1993) and Falconer et al. (1998) that network brightenings over unipolar regions only appear to be present due to a failure to resolve the opposite polarity flux in the magnetograms. That argument does not seem to hold in this situation.

However other regions at (25,35) and (60,40) do show brightenings over bipolar magnetic field regions. Following the definition of Dowdy (1993) these are considered to be locations of network loops. The expansion of the bright network area in these locations indicates the expansion of network loops as they arch up into the corona. Furthermore, both loops and funnels must reach coronal temperatures as the expansion of these features in the bright network can be seen all the way from O III up to Si X at $\log T_e=6.1$ K (see Fig. 4). Note, however, that certain bright points in the low temperature lines do not show equivalent brightenings in the higher temperature lines, e.g. at (140, 175), (185, 185), (200, 160). These brightenings are present in O V (Fig. 5), but not in the higher temperature Si VIII line. They can similarly be seen in *all* the low temperature lines in Fig. 4 but not in the high temperature lines. These brightenings are interpreted as internally heated network loops without any strong thermal connection with the large-scale corona. In fact, the brightening at (140, 175) may be occurring over a unipolar region, suggesting a possible low temperature funnel structure.

3.3. Radiative losses

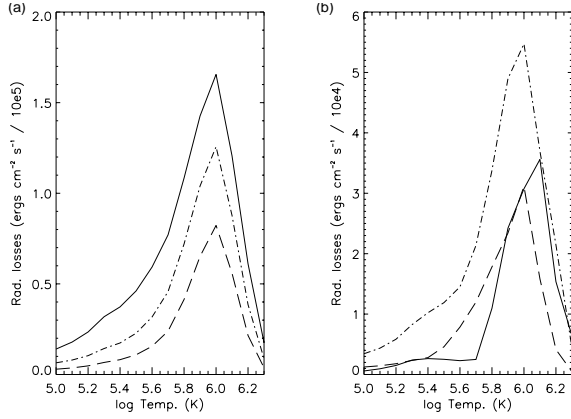
In Table 3 we present the total radiative losses calculated using our emission measures and the radiative loss function of Cook et al. (1989). The radiative loss function was scaled to the coronal abundances of Feldman et al. (1992). The radiative losses have been integrated over the temperature range $\log T_e=5.0-6.3$ K (see Fig. 6(a)). Scaling these radiative losses to the area fractions shown in Fig. 3 for the three regions results in the curves shown in Fig. 6(b). From this figure it is clear that the bright network contributes little to radiative losses below $\log T_e=5.7$ K, due to its small spatial extent at these temperatures. However, between $\log T_e=5.7$ and $\log T_e=6.3$ as much as 30% of the total radiative losses is accounted for by bright network emission, and thus by continuous layers in a stratified atmosphere as suggested in the previous section. The integrated value of the scaled radiative losses over $\log T_e=5.0-6.3$ K is shown in the final column of Table 3. The sum of these integrated values gives a value of 5.46×10^5 ergs $\text{cm}^{-2} \text{s}^{-1}$ for the whole quiet Sun, agreeing well with the value of 6×10^5 ergs $\text{cm}^{-2} \text{s}^{-1}$ calculated by Dere & Mason (1993).

3.4. Geometry of the emission

Chae et al. (1998) showed that the variation with temperature of the relative cross-sectional area of a flux tube can be estimated from measurements of redshift velocity, if the pressure is presumed constant in the transition region and if the mass flux

Table 3. The distribution of magnetic field and radiative losses within the bright network, normal network and internetwork.

| Region | O v Area (%) | Mean Magnetic Field (Gauss) | Max Magnetic Field (Gauss) | Fraction of Total Magnetic Field (%) | Rad. Losses (ergs cm ⁻² s ⁻¹) | Scaled Rad. Losses (ergs cm ⁻² s ⁻¹) |
|----------------|--------------|-----------------------------|----------------------------|--------------------------------------|--|---|
| Bright Network | 7.07 | 16.14 | 330.70 | 10.50 | 9.23 × 10 ⁵ | 1.39 × 10 ⁵ |
| Normal Network | 58.77 | 10.77 | 288.46 | 58.91 | 5.93 × 10 ⁵ | 2.80 × 10 ⁵ |
| Internetwork | 34.16 | 9.51 | 77.61 | 30.59 | 3.46 × 10 ⁵ | 1.27 × 10 ⁵ |

**Fig. 6a and b.** a The radiative losses shown for each of the three regions; bright network (solid line), normal network (dot-dash line) and cell (dashed line). b The scaled radiative losses for the same regions.

carried by the downward motion is conserved along the flux tube.

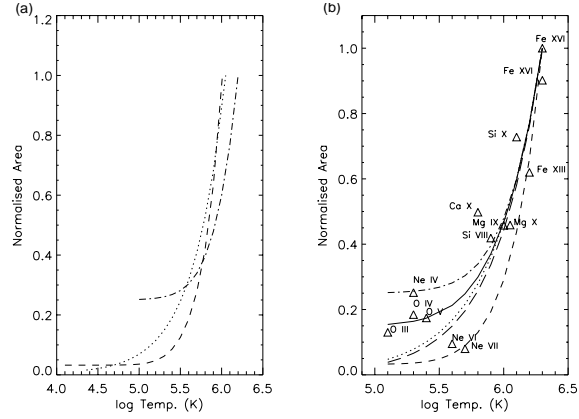
Using this technique they were able to produce estimates of the relative area of a flux tube from their redshift measurements which they then fitted with the functional form (see Dowdy et al., 1987 and Rabin, 1991);

$$A(T)/A(T_h) = [1 + (\Gamma^2 - 1)(T/T_h)^\nu]^{1/2}/\Gamma \quad (4)$$

where $A(T)$ is the area of the flux tube as a function of temperature, $A(T_h)$ is the area at the hot end of the flux tube (in their case $T_h = 10^6$ K), ν is the value of the shape factor and Γ is the amount of constriction of the flux tube, $\Gamma = A(T_h)/A(T_c)$, with $A(T_c)$ being the area at the cool (usually chromospheric) end. Γ is also sometimes referred to as the loop expansion factor. The shape factor ν , as its name suggests, determines the shape of the flux tubes (see Dowdy et al., 1985, 1987).

From their redshift measurements Chae et al. (1998) calculated values of $\Gamma = 31$ and $\nu = 3.6$ for the constriction and shape factor respectively. Inserting these values into Eq. 4 gives the curve with the short dashes shown in Fig. 7(a). Similarly, using other redshift values from Brekke et al. (1997) we were able to calculate values of $\Gamma = 114$ and $\nu = 2.2$ and to produce the curve with the dots shown in Fig. 7(a). Rabin (1991) showed that the hotter transition region plasma ($5.0 \leq \log T_e \leq 6.0$) can be explained as a conductive transition between the corona and the chromosphere if he modelled a bowl(horn) shaped funnel with $\Gamma = 4$, $\nu = 2.5$ and $T_h = 10^{6.2}$ K. Using these estimates of Γ , ν and T_h in Eq. 4 gives the dot-dash line shown in Fig. 7(a).

In Fig. 7(b) we plot as triangle symbols the normalised area of bright network emission as a function of temperature. Fitting

**Fig. 7a and b.** a Estimates of normalised cross-sectional areas calculated from the redshift values of Brekke et al. (1997), dotted line, Chae et al. (1998), dashed line and from the Rabin (1991) model parameters (dot-dash line). b The normalised area of the bright network emission overplotted with a thin black line fit, using the function in Eq. 4. Also plotted are the equivalent estimated areas from the Rabin coefficients (dot-dash line), the Brekke coefficients (dotted line) and the Chae coefficients (dashed line) together with a fit to the observed bright network area above $\log T_e = 5.6$ K (long dashes).

these values with the functional form shown in Eq. 4, where in this case we chose $T_h = 10^{6.3}$ K, the temperature of Fe XVI, gives values of $\Gamma = 6.7$ and $\nu = 2.3$. Inputting these values back into Eq. 4 results in the curve shown in Fig. 7(b) as a continuous thin black line. Using the estimated values of Γ and ν from Chae et al. (1998), Brekke et al. (1997) and Rabin (1991), but with $T_h = 10^{6.3}$ K to compare with our results, gives the different dashed and dotted curves shown in Fig. 7(b).

It is clear from Fig. 7(b) that the estimated cross-sectional areas are similar in shape to the fit of our measured bright network emission areas. This is particularly true in the case of the areas estimated from the Brekke et al. (1997) redshifts, especially at temperatures above $\sim \log T_e = 5.6$ K. If we only fit the measured values above $\log T_e = 5.6$ K with the functional form of Eq. 4 (i.e. if we remove the effects of the low temperature lines) we obtain the curve shown in Fig. 7(b) with long dashes. We note that this curve has a very similar shape to the estimated areas from the Brekke et al. (1997) redshifts as can be seen in the figure. This new curve has $\nu = 2.36$ and a large $\Gamma = 2625$. The fact that the estimated cross-sectional areas (from Chae et al., 1998 and Brekke et al., 1997) have a similar shapes to the observed area expansion of the bright network strongly suggests that what we are seeing in these bright network regions (at least above $\sim \log T_e = 5.6$ K) is an expansion of flux tubes, either in

loops or funnels, with a corresponding downflow of redshifted material.

Some recent work of Teriaca et al. (1999), Peter (1999) and Peter & Judge (1999) has found evidence for a net blueshift above temperatures of $\log T_e=5.7$ K, in contradiction to Chae et al. (1998) and Brekke et al. (1997). Peter (1999) discusses these blueshifts and points out that they may be evidence for downward propagating waves induced by nanoflares in loops, similar to the model by Hansteen (1993). This is also the conclusion reached by Teriaca et al. (1999). However Peter (1999) mentions another possibility, in that the observed blueshifts may be the solar wind in the transition region. He further suggests that the redshifted material may originate in the cool loops below temperatures of 5×10^5 K, with the higher temperature blueshifted material (the slow solar wind) originating in the regions in between (i.e. the coronal funnels). In producing the cross-sectional estimates of the Brekke et al. (1997) redshifts we assumed that there was a constant *downward* flux present. However if above 5×10^5 K there are blueshifts present (as shown by Peter & Judge, 1999 etc.) we can assume that above this temperature there is a constant *upward* flux of material. If so, then the fact that the estimated cross-sectional areas from Brekke et al. (1997) above $\sim 5 \times 10^5$ K (i.e. $\log T_e=5.7$) are so similar to our fits of the observed bright network emission area would lead us to conclude that if there were blueshift velocities present, of the same magnitude as the Brekke et al. (1997) redshifts above $\sim 5 \times 10^5$ K, then they would provide the same close correspondence with our observed results.

4. Conclusions

In this paper we discuss the quiet Sun in terms of three intensity distributions; the internetwork, the 'normal' network and the bright network. From an analysis of emission measures we find that the slopes between temperatures of $5.4 \leq \log T_e \leq 6.0$ are different in each of the three intensity regions. The change in the slope with intensity suggests that there are different density structures present in each region. An analysis of the area of emission in each distribution suggests that in the combined network region (normal network and bright network) there are two populations of network structures, a low transition region group and a coronal group.

Using magnetograms, we have found that the bright network is composed of coronal funnels and network loops. Furthermore these loops and funnels are continuous structures reaching coronal temperatures, as their expansion can be seen all the way from O III up to Fe XVI. For $\log T_e > 5.7$, up to 30% of the total radiative losses are attributed to the bright network emission, and thus by continuous layers in a stratified atmosphere. The structure of the combined network is seen to change substantially above a temperature of approximately $\log T_e=5.7$.

Cross-sectional areas estimated from redshift values suggest that what is seen in bright network regions is the result of flux tube expansion in loops and funnels into the corona, accompanied by a downflow or possibly upflow of material.

Future work in this area would involve time series of rasters to examine the variation of network structures with time. These rasters combined with simultaneous magnetogram observations could help to further identify the 'Dowdy' component in the network by allowing a more comprehensive statistical analysis to be carried out.

Acknowledgements. We would like to thank the CDS teams at Goddard Space Flight Center and at the Rutherford Appleton Laboratory for their help in obtaining the data. CDS is part of SoHO, the Solar and Heliospheric Observatory, which is a project of international cooperation between ESA and NASA. EOS is grateful to PPARC for financial support, and PTG acknowledges the award of a studentship from the Department of Education for N.Ireland. This work has been supported by the Nuffield Foundation (NUF-NAL)

References

- Arnaud M., Rothenflug R., 1985, A&AS 60, 425
 Athay R.G., 1981, ApJ 249, 340
 Athay R.G., 1982, ApJ 263, 982
 Brekke P., Hassler D.M., Wilhelm K., 1997, Sol. Phys. 175, 349
 Chae J., Yun H.S., Poland A.I., 1998, ApJS 114, 151
 Cook J.W., Cheng C.-C., Jacobs V.L., Antiochos S.K., 1989, ApJ 338, 1176
 Del Zanna G., Bromage B.J.I., Dere K., Pike C.D., 1997, CDS software note no. 50
 Dere K.P., Mason H.E., 1993, Sol. Phys. 144, 217
 Dere K.P., Landi E., Mason H.E., Monsignori-Fossi B.C., Young P.R., 1997, A&AS 125, 149
 Dowdy J.F., 1993, ApJ 411, 406
 Dowdy J.F., Moore R.L., Wu S.T., 1985, Sol. Phys. 99, 79
 Dowdy J.F., Rabin D., Moore R., 1986, Sol. Phys. 105, 35
 Dowdy J.F., Emslie A.G., Moore R.L., 1987, Sol. Phys. 112, 255
 Falconer D.A., Moore R.L., Porter J.G., Hathaway D.H., 1998, ApJ 501, 386
 Feldman U., 1987, ApJ 320, 426
 Feldman U., Mandelbaum P., Seely J.F., Doschek G.A., Gursky H., 1992, ApJS 81, 387
 Gabriel A.H., 1976, Phil. Trans. R. Soc. Lond. A. 281, 339
 Gallagher P.T., Phillips K.J.H., Harra-Murnion L.K., Keenan F.P., 1998, A&A 335, 733
 Griffiths N.W., Fisher G.H., Woods D.T., Siegmund O.H.W., 1999, ApJ 512, 992
 Gupta L., Sortrakul T., 1998, Pattern Recognition 31, No. 3, 315
 Habbal S.R., Dowdy J.F., Withbroe G.L., 1990, ApJ 352, 333
 Habbal S.R., Grace E., 1991, ApJ 382, 667
 Hansteen V.H., 1993, ApJ 402, 741
 Harrison R.A., Sawyer E.C., Carter M.K., et al., 1995, Sol. Phys. 162, 233
 Patsourakos S., 1999, ApJ 522, 540
 Peter H., 1999, ApJ 516, 490
 Peter H., Judge P.G., 1999, ApJ 522, 1148
 Rabin D., 1991, ApJ 383, 407
 Raymond J.C., Doyle J.G., 1981, ApJ 247, 686
 Reeves E.M., Vernazza J.E., Withbroe G.L., 1976, Phil. Trans. R. Soc. Lond. A. 281, 319
 Scherrer P.H., Bogart R.S., Bush R.I., et al., 1995, Sol. Phys. 162, 129
 Teriaca L., Banerjee D., Doyle J.G., 1999, A&A 349, 636
 Vernazza J.E., Avrett E.H., Loeser R., 1981, ApJS 45, 635
 Weszka J.S., Rosenfeld A., 1979, IEEE Transactions on Systems, Man, and Cybernetics. SMC-9, No. 1, 38